Three-dimensional Modeling of the Interaction of a Bubble pair with a Rigid Wall using Boundary Integral Method

Imad A. Aziz

1Department of Mathematics, College of Science, Salahaddin University-Erbil, Erbil, Kurdistan Region, Iraq

ABSTRACT

This study examines the three-dimensional dynamics of two gas bubbles near a horizontal rigid wall, focusing on how inter-bubble distance affects their shape, size, and jet formation. The Boundary Integral Method (BIM) with a novel local smoothing technique is employed. Critical parameters including jet velocity, bubble centroid movement, bubble radius, and collapse time are computed for each bubble to understand their interaction dynamics comprehensively. The velocity vector field and pressure distribution surrounding the bubbles are analyzed, providing detailed insights into the fluid dynamics. The findings demonstrate that inter-bubble distance significantly influences their interaction and overall behavior. These results advance the understanding of bubble dynamics near rigid boundaries, with potential applications across various scientific and engineering disciplines.

1.Introduction

Studying the behavior of gas bubbles in the vicinity of rigid boundaries is of fundamental interest in many applications including marine environment and biomedical engineering. Understanding this phenomenon is vital for improving various operations like mineral flotation, water purification, and medical ultrasonic imaging. In marine environment, the behavior of bubbles concerning the seabed or the ship hull influences underwater noise, which has impacts on the life of marine organisms (Deane and Stokes, 2002). Also, the study of bubble dynamics is relevant in the application of ultrasound imaging where microbubbles are used as contrast agents to improve the visualization of blood vessels and tissues (Ferrara et al., 2007). In the petroleum industry, bubble dynamics play a crucial role in enhanced oil recovery, particularly in gas injection techniques, where the behavior of bubbles significantly impacts the efficiency of oil displacement (Church, 1995). In addition, bubble dynamics play a crucial role in chemical engineering processes like gas-liquid reactions, where the bubble behavior and interaction with solid surfaces affect the reaction kinetics and product yield (Tsouris and Tavlarides, 1994). In wastewater treatment, the aeration process in which air bubbles are introduced into the water to stimulate microbial action is greatly influenced by the behavior of the bubbles near surfaces (Deen et al., 2004).

Two gas bubbles' behavior has also been studied by researchers. These include numerical simulation of two bubbles located horizontally near a free surface (Zhang and Xiong-Liang, 2008, Wang et al., 2003, Xi, 2004, Yao et al., 2007), numerical investigation of a pair of bubbles placed vertically near a free surface (Li et al., 2012, Saleki-Haselghoubi et al., 2024), boundary integral simulation of the motion and deformation of bubbles with viscous effects in an infinite domain (Zhang and Ni, 2014), computational analysis of two bubbles set vertically near a rigid wall (Han et al., 2018), and study of a pair of acoustic bubbles placed in parallel near a horizontal solid wall (Ye et al., 2015).

Recently the dynamics of bubbles under different conditions have been investigated. Specifically, a new extended Laplacian smoothing technique has been introduced for boundary element analysis, aimed at enhancing the accuracy of modeling 3D bubble dynamics (Jund et al., 2024). Another research examined the impact of non-isothermal phase changes on the cavitation bubble dynamics, emphasizing the challenges posed by these variations (Choi et al., 2024). Furthermore, shock wave induced by the collapse of randomly distributed bubble clusters and the resulting pressure loads on the near walls was examined (Yang et al., 2024). The researchers also carried out theoretical and numerical studies to explore the interaction between Bjerknes and buoyancy forces during underwater explosion near a free surface and illustrated the coupled dynamics involved. These works contribute valuable knowledge to the broader understanding of bubble behavior in various environments pertinent to the current study (Wang et al., 2024).

Despite recent advancements, significant gaps remain in our understanding of the dynamics of two gas bubbles near rigid walls, especially concerning how bubble size, wall geometry, and fluid properties affect their overall behavior. This paper seeks to fill some of these gaps by presenting computational results on the dynamics of two gas bubbles near a rigid wall, providing insights into the underlying mechanisms and implications for various applications.

The rest of the paper is arranged as follows. In Section 2, the mathematical model is presented. Section 3 deals with the numerical implementation, and Section 4 discusses the local mesh smoothing technique. In Sections 5 and 6, the results are presented and discussed, including validation of the developed BIM code, two bubbles dynamics, and pressure and velocity fields of the liquid around the bubbles. Finally, in Section 7, conclusions are given.

2 Mathematical model

Consider initially two spherical identical gas bubbles inside an incompressible, Newtonian, and inviscid liquid domain Ω located near a horizontal rigid wall. The bubbles are located at

$(d^*/2, 0,0)$ and $(-d^*/2, 0,0)$ of the Cartesian coordinates system xyz and the horizontal wall is located on the plane $z = -l^*$. The bubbles and the wall surfaces are denoted by $S_{b1} = S_{b1}(t)$, $S_{b2} = S_{b2}(t)$, and S_w, respectively where $\partial\Omega(t) = S_{b1}(t) + S_{b2}(t) + S_w$, and t denotes time (see Fig.1). In addition, the dimensionless horizontal distance between the center of initial bubbles denoted by $d^* = d/R_m$ and shortest dimensionless vertical distances from the center of each bubble to the wall is $l^* = l/R_m$ as shown in Fig. 1. Here, R_m is the maximum radius of the bubbles. Since the initial radius of each bubble is

the same, R_m remains the same for the bubbles. The liquid flow is considered irrotational and assumed to be incompressible, Newtonian, and inviscid. Based on the potential flow theory, the velocity field is defined as $\vec{u} = \vec{\nabla}\varphi$, where φ denotes velocity potential that satisfies the Laplace's equation $\Delta\varphi = 0$. By utilizing the fundamental solution, known as Green's function, for Laplace's equation along with Green's second identity, the Laplace's equation can be expressed in the form of a surface integral (Duffy, 2015, Katsikadelis, 2016),
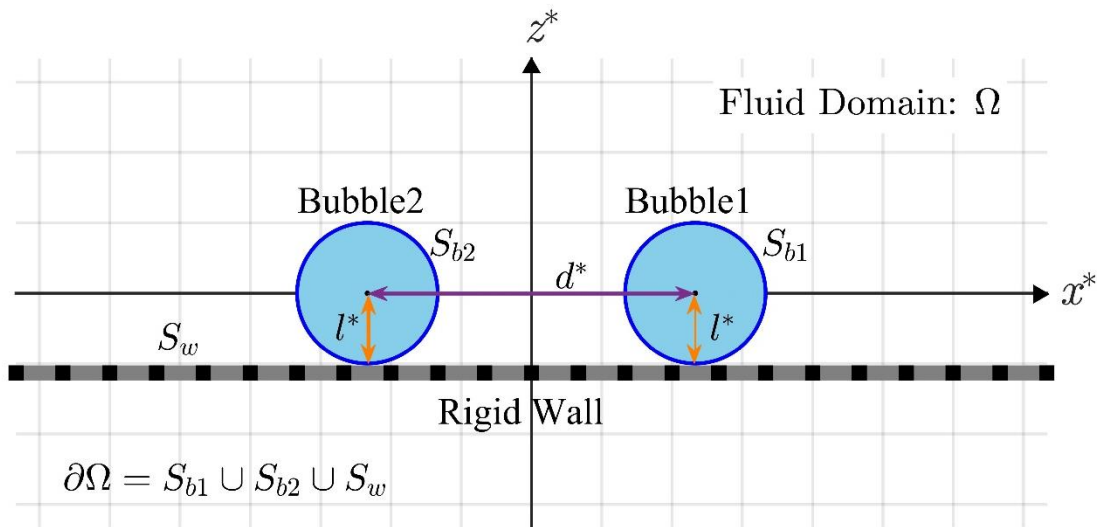
Fig. 1 Schematic front view of two bubbles near a horizontal rigid wall.

$$c(\vec{P},t)\varphi(\vec{P},t) = \int_{\partial\Omega(t)} \left(\frac{\partial\varphi(\vec{Q},t)}{\partial\hat{n}} G(\vec{P},\vec{Q}) - \varphi(\vec{Q},t)\frac{\partial G(\vec{P},\vec{Q})}{\partial\hat{n}} \right) dS(\vec{Q}), \quad (1)$$

where $\vec{P} = (x, y, z)$ is the field point, $\vec{Q} = (x_0, y_0, z_0)$ is the source point, and $c(\vec{P},t)$ is the solid angle at the field point $\vec{P}$, which is given as

$$c(\vec{P},t) = \begin{cases} 4\pi & \vec{P} \in \Omega \\ 2\pi & \vec{P} \in \partial\Omega(t) \end{cases},$$

for a smooth surface, whereas for a non-smooth surface, we used a formula known as the 4π rule (Li et al., 2012). Furthermore, $\hat{n}$ is the outward normal from the flow, and $G(\vec{P},\vec{Q})$ denotes the Green's function defined as

$$G(\vec{P},\vec{Q}) = \frac{1}{\|\vec{P}-\vec{Q}\|}.$$

Following the adiabatic law, Young–Laplace equation, unsteady Bernoulli's equation, and applying the far field boundary conditions, the dynamic boundary conditions on the bubble surface is derived as (Wang et al., 2022, Aziz et al., 2019),

$$\frac{d\varphi}{dt} = \frac{p_\infty - p_c}{\rho} + \frac{1}{2}|\vec{\nabla}\varphi|^2 - gz + \frac{\sigma}{\rho}(\vec{\nabla}\cdot\hat{n}) - \frac{p_0}{\rho}\left(\frac{V_0}{V}\right)^\lambda,$$

where, p_∞ is the hydrostatic pressure at the far field of the liquid, p_c is the condensable vapor pressure, σ is the surface tension coefficient, $\vec{\nabla}\cdot\hat{n}$ is the curvature, p_0 denotes the initial gas

pressure inside the bubble and λ is the ratio of specific heats of the gas. In addition, ρ is the fluid density, V is the intsantanous volume of bubble, V_0 is the initial volume of bubble, g is the gravitational acceleration, z is z-coordinate of the point $\vec{r} = (x, y, z)$.

On the other hand, the kinematic boundary condition on the bubbles surface S_b requires a liquid particle to remain on them, i.e.,

$$\frac{d\vec{r}}{dt} = \vec{\nabla}\varphi, \quad \vec{r} \in S_b.$$

The boundary condition on the surface of the wall, S_w, satisfying the no-penetration condition is

$$\frac{\partial \varphi}{\partial \hat{n}} = 0.$$

The maximum bubble radius R_m and $\Delta p = p_\infty - p_c$ are considered as the reference scales to normalize the variables. Then the above equations get reduced to

$$\frac{d\varphi_*}{dt_*} = 1 + \frac{1}{2}|\vec{\nabla}^*\varphi_*|^2 - \delta_*^2 z_* + \sigma_* \kappa_* - \varepsilon\left(\frac{V_0}{V}\right)^\lambda, \quad (2)$$

$$\frac{d\vec{r}_*}{dt_*} = \vec{\nabla}^*\varphi_*, \quad (3)$$

$$\frac{\partial \varphi_*}{\partial \hat{n}} = 0,$$

where $\varepsilon = p_0/\Delta p$. In the remainder of the paper all variables and parameters are non-dimensional; however, for simplicity, the asterisk has been omitted.

3 Numerical implementation

In order to solve the boundary integral equation (1), first, the domain boundary $\partial\Omega$ (surface of bubbles and wall) is divided into a collection of n_e boundary elements, denoted by E^i,

$$\partial\Omega = \bigcup_{i=1}^{n_e} E^i \text{ and } E^i \cap E^l \equiv \emptyset \quad \text{when } i \neq l,$$

where n_e is the number of boundary elements that span the domain boundary $\partial\Omega$. The boundary elements are taken to be simple, using a single standard triangular element in 2-D. Since the surface of bubbles and the rigid wall are smooth, the integrals over $\partial\Omega$ can be transformed into sums of integrals over the boundary elements E^i, i.e.,

$$c(\vec{P}, t)\varphi(\vec{P}, t) = \sum_{i=1}^{n_e} \int_{E_i} \left(\frac{\partial \varphi(\vec{Q}, t)}{\partial \hat{n}} G(\vec{P}, \vec{Q}) \right.$$
$$\left. - \varphi(\vec{Q}, t) \frac{\partial G(\vec{P}, \vec{Q})}{\partial \hat{n}} \right) dE_i, \quad (4)$$

Because the boundary elements are simple triangles, each defined by a group of three element nodes, the collection of the nodes of the elements are defined by the global grid nodes.

Next, the surface of each boundary element is described in a parametric form by mapping the triangular element from three-dimensional space to a right isosceles triangle in the $\xi\eta$ parametric plane. The position vector $\vec{r}$, the velocity potential φ and its normal derivative $\psi = \partial\varphi/\partial n$ are interpolated linearly along the triangle of boundary element E^k

$$\vec{r}^k = \xi\vec{r}_1^k + \eta\vec{r}_2^k + (1 - \xi - \eta)\vec{r}_3^k,$$
$$\varphi^k = \xi\varphi_1^k + \eta\varphi_2^k + (1 - \xi - \eta)\varphi_3^k,$$
$$\psi^k = \xi\psi_1^k + \eta\psi_2^k + (1 - \xi - \eta)\psi_3^k.$$

Therefore, Eq. (4) can be represented as

$$c_k\varphi_k = \sum_{i=1}^{e_n} \sum_{j=1}^{3} \left(C_j^i \psi_j^i - D_j^i \varphi_j^i \right), \quad k = 1, \ldots, n_g, \quad (5)$$

where n_g is the number of global nods in the grid, and the influence coefficients C_j^i and D_j^i are surface integral over a parametric plane of boundary element E^i according to local function node j. By combining the nodes from all neighboring triangles that share a common node and after performing summation, Eq. (5) becomes,

$$c_k\varphi_k = \sum_{i=1}^{n_g} (A_i\psi_i - B\varphi_i), \quad k = 1, \ldots, n_g, \quad (6)$$

where A_i and B_i are the altered influence coefficients due to the summation of triangles around their common node. Equation (6) can be expressed in matrix form as

$$\mathbf{c} \cdot \boldsymbol{\varphi} = \mathbf{A}\boldsymbol{\psi} - \mathbf{B}\boldsymbol{\varphi}, \quad (7)$$

where $\mathbf{A}$ and $\mathbf{B}$ are the $n_g \times n_g$ influence coefficient matrices. The diagonal elements of $\mathbf{A}$ are integrated analytically, while the non-diagonal elements of $\mathbf{A}$ and $\mathbf{B}$ are calculated numerically using seven-point Gaussian quadrature.

Rewriting the matrix form (7) as a linear system

by putting unknown values in LHS and known values in RHS (where $\psi = 0$ on the wall and φ on the bubbles are known, while ψ on the bubbles and φ on the wall are unknown), then

$$\begin{bmatrix} \mathbf{A}_{bb} & -\mathbf{B}_{bw} \\ \mathbf{A}_{wb} & -\mathbf{B}_{ww} \end{bmatrix} \begin{bmatrix} \mathbf{\Psi}_b \\ \mathbf{\varphi}_w \end{bmatrix}$$
$$= \begin{bmatrix} \mathbf{B}_{bb} & -\mathbf{A}_{bw} \\ \mathbf{B}_{wb} & -\mathbf{A}_{ww} \end{bmatrix} \begin{bmatrix} \mathbf{\varphi}_b \\ \mathbf{\Psi}_w \end{bmatrix}. \qquad (8)$$

By solving the linear system of equations (8), the normal velocity ψ on the bubbles is found. The tangential velocity of φ can be obtained using linear interpolation of the velocity potential φ along each triangular element (Wang and Manmi, 2014, Wang et al., 2015). Then,

$$\vec{u} = \vec{u}_\parallel + \vec{u}_\perp,$$

where $\vec{u}_\parallel$ is the normal velocity and $\vec{u}_\perp$ is the tangential velocity.

The positions of the bubbles grid nodes $\vec{r}$ and the velocity potential φ are updated using (2) and (3). The following predictor-corrector scheme is used for the position,

$$\vec{r}_p = \vec{r}_i + \mathrm{d}t_i\,\vec{u}_i,$$
$$\vec{r}_{i+1} = \vec{r}_i + 0.5\,\mathrm{d}t_i[\vec{u}_i + \vec{u}_p].$$

For the velocity potential let

$$f(\vec{r}_i) = 1 + 0.5|\vec{\nabla}\varphi(\vec{r}_i)|^2 - \delta^2 z(\vec{r}_i) + 2\sigma\kappa(\vec{r}_i)$$
$$- \varepsilon\left(\frac{V_0}{V(\vec{r}_i)}\right)^\lambda,$$

then

$$\varphi_p = \varphi_i + \mathrm{d}t_i\,f(\vec{r}_i),$$
$$\varphi_{i+1} = \varphi_i + 0.5\,\mathrm{d}t_i\,(f(\vec{r}_i) + f(\vec{r}_p))),$$

where $\vec{r}_{i+1}$ and φ_{i+1} are the position $\vec{r}$ and velocity potential φ at the next time step, respectively, and $\mathrm{d}t_i$ is time-step chosen as follows to save the CPU time,

$$\mathrm{d}t_i = \frac{\mathrm{d}\varphi}{\max|f(\vec{r}_i)|}.$$

Here, $\mathrm{d}\varphi$ is a constant and κ is the mean curvature calculated by the algorithm given in (Dong and Wang, 2005).

In this section, the procedure of calculating the pressure and velocity fields of the fluid around the two bubbles in zx-plane is given. Based on the potential flow theory, the pressure field p in the liquid domain surrounding the bubbles can be found using the unsteady Bernoulli equation as

follows (Wu, 1998, Tanizawa, 1995),

$$p = 1 - \frac{\partial\varphi}{\partial t} - \frac{1}{2}|\vec{\nabla}\varphi|^2 - \delta^2 z. \qquad (9)$$

The liquid domain around bubbles and bounded at the bottom by the rigid wall is discretized to m_e elements with m_f nodes in the zx-plane. The calculation of φ_t in fluid needs the values of φ_t and $\partial\varphi_t/\partial n$ on the boundaries. Using the unsteady Bernoulli equation,

$$\varphi_t = 1 - \frac{1}{2}|\vec{\nabla}\varphi|^2 - \delta^2 z - \varepsilon\left(\frac{V}{V_0}\right)^\lambda, \qquad (10)$$

and to calculate $\partial\varphi_t/\partial n$ on the bubble surface, the BIM (1) is used,

$$c(\vec{P}, t)\varphi_t(\vec{P}, t)$$
$$= \int_{\partial\Omega(t)} \left(\frac{\partial\varphi_t(\vec{Q})}{\partial\hat{n}} G(\vec{P}, \vec{Q}) \right.$$
$$\left. - \varphi_t(\vec{Q}, t)\frac{\partial G(\vec{P}, \vec{Q})}{\partial\hat{n}} \right) dS(\vec{Q}). \qquad (11)$$

Finally, the boundary integral equation is used to find φ_t,

$$\varphi_t(\vec{r}_i) = \frac{1}{4\pi}\sum_{j=1}^{N} \left(\frac{\partial\varphi_t(\vec{P}_j)}{\partial n}A_{ij} - \varphi_t(\vec{P}_j)B_{ij} \right), \quad i = 1; m_f, \qquad (12)$$

and to evaluate φ_x, φ_y, and φ_z at a fluid point,

$$\varphi_x(\vec{r}_i) = \frac{1}{4\pi}\sum_{j=1}^{N} \left(\frac{\partial\varphi_x(\vec{P}_j)}{\partial n}A_{ij} - \varphi_x(\vec{P}_j)B_{ij} \right), \quad i = 1; m_f, \qquad (13)$$

$$\varphi_y(\vec{r}_i) = \frac{1}{4\pi}\sum_{j=1}^{N} \left(\frac{\partial\varphi_y(\vec{P}_j)}{\partial n}A_{ij} - \varphi_y(\vec{P}_j)B_{ij} \right), \quad i = 1; m_f, \qquad (14)$$

$$\varphi_z(\vec{r}_i) = \frac{1}{4\pi}\sum_{j=1}^{N} \left(\frac{\partial\varphi_z(\vec{P}_j)}{\partial n}A_{ij} - \varphi_z(\vec{P}_j)B_{ij} \right), \quad i = 1; m_f \qquad (15)$$

where $\vec{r}_i$ is the coordinates of the ith fluid point, $\vec{P}$ is the boundary point, and

$$A_{ij} = \int_E G(\vec{r}_i, \vec{P}_j)dE(\vec{P}), \qquad (16)$$

$$B_{ij} = \int_E \frac{\partial G(\vec{r}_i, \vec{P}_j)}{\partial n}dE(\vec{P}). \qquad (17)$$

After finding φ_t and $\nabla\varphi = (\varphi_x, \varphi_y, \varphi_z)$ in the fluid domain around the bubbles, they are emplyed to

find the pressure at fluid points using (9).

4 Local mesh smoothing technique

Surface smoothing is essential for maintaining the stability of dynamic modules. In this work, we employ a modified version of Laplace smoothing, an iterative process that relocates each mesh node to the barycenter of its neighbors. This process comprises two substeps: shrinking and expansion (Aziz et al., 2019, Rypl and Nerad, 2016).

Additionally, we introduce a novel technique called Local Mesh Smoothing (LMS). This method aims to smooth a subgroup of nodes belonging to the global nodes of bubbles boundaries.

Let

$$\mathbf{X} = \left\{\vec{P}_i\right\}_{i=1}^{n},$$

be the sequence of all nodes on the bubble surface, where n is the number of bubble nodes, and let

$$\mathbf{S} = \left\{\vec{Q}_i : \vec{Q}_i \in \mathbf{X} \wedge G(\vec{Q}_i) \leq M\right\}_{i=1}^{m},$$

be a subgroup of $\mathbf{X}$, where $M \in \mathbb{R}$ and $G: \mathbb{R}^3 \longrightarrow \mathbb{R}$ is the same function.

Also, suppose that $H: \mathbf{X} \longrightarrow \mathbb{Z}_m$ is the one-to-one function from nodes to its index in triangulation; therefore,

$$H(\mathbf{S}) = \mathbf{S}_h \subseteq \mathbb{Z}_m,$$

which can locate the nodes in $\mathbf{S}$ by

$$\mathbf{S} = H^{-1}(\mathbf{S}_h),$$

Then, the smooth solution is applied only to target nodes on the bubble surface (often part of the jet surface). This technique may occasionally create a dividing line between two areas due to differences in shape size, which arise from applying smoothing in one area and not in the other. However, with LMS, the likelihood of this issue is virtually eliminated. LMS operates in two steps during each iteration: one step shrinks the size while the other expands it, ensuring that the overall shape size remains nearly constant.

5 Validation

The validation of a numerical method is essential to ensure the accuracy of the numerical results. In this section, the current numerical results associated with two identical bubbles oscillating near each other in an infinite fluid domain is evaluated through the comparison with numerical results of Wang and Khoo (Wang and Khoo, 2004). The parameters are taken as in (Wang and Khoo, 2004), where the initial bubble radius are $R_0 = 0.1391$, the vertical distance between theo bubbles is set to $d^* = 1.8$, $\delta = 0$ and $\varepsilon = 120$. Fig. 2(a) presents the obtained result, which is congruent with the result (Fig. 2c) of Wang and Khoo (Wang and Khoo, 2004) in terms of shape, size, and collapse time. Besides, our numerical results associated with two bubbles oscillating near each other in an infinite fluid domain is also validated by comparing with the numerical result of Li et al. (Li et al., 2012). The parameters set same as those given in (Li et al., 2012), where $R_0 = 0.1651$, $d^* = 1.5$, $\delta = 0$ and $\varepsilon = 100$. The shape in Fig. 2(b) is our result, which is smoother than the result in (Li et al., 2012) (Fig. 2d). Also, unlike the result in (Li et al., 2012) shown in Fig. 2(d), the bubbles in our simulations have reached the final stage of collapse.
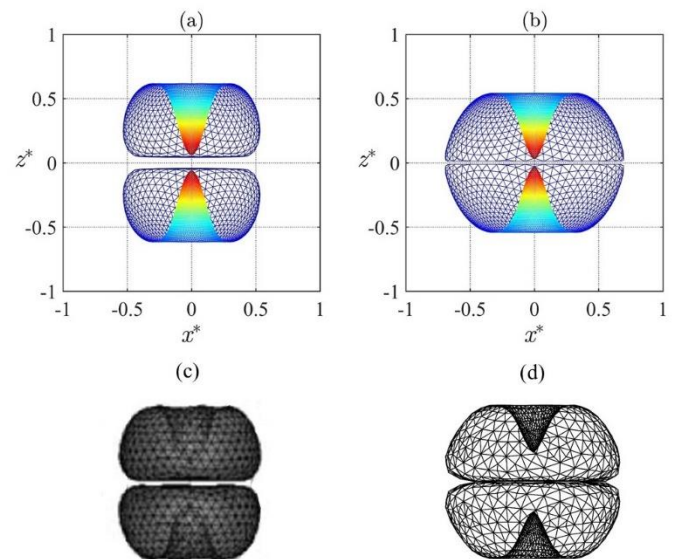
Fig. 2 Comparison of the current 3D BEM results related to the 3D bubbles shape at the end of collapse phase for (a) $d^* = 1.8$ and (b) $d^* = 1.5$ with numerical results of (c) Wang and Khoo (2004) and (d) Li et al. (2012).

To further enhance our confidence in the numerical modeling, we considered a problem where two bubbles oscillate near a horizontal solid wall with the dimensionless distance between the bubbles being 20 ($d^* = 20$). This distance likely reduces the effect of two bubbles on each other, meaning their influence on one another is largely negligible. The results are illustrated in Fig. 3, which demonstrates that the two bubbles adopt shapes similar to those observed when positioned individually near a horizontal solid wall. A slight deviation in the direction of the bubble jet is observed, directing towards the other bubble. This suggests that our numerical results are reliable.
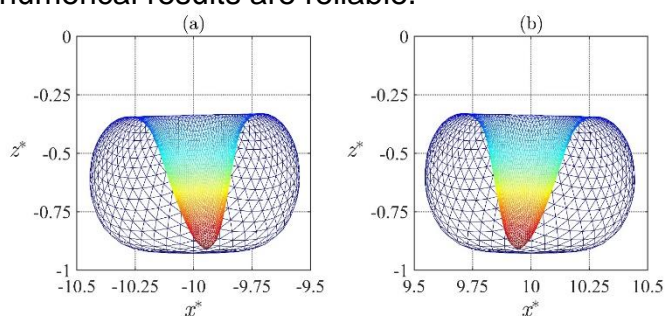
Fig. 3 Bubbles shape at the end of collapse phase as they oscillate near a horizontal rigid wall for $d^* = 20$; (a) left bubble and (b) right bubble.

6 Results and discussions

To numerically study the dynamics of two bubbles near a horizontal solid wall, where each bubble is one unit away from the solid wall, i.e. ($l^* = 1$) as shown in Fig. 1, five different distances d^* between the centers of the two bubbles are considered, and the effect of these distances on the shape of the bubbles and their jets are sought. In addition, the effects of the distance d^* on the bubble radius, jet velocity, bubble centroid motion, bubble lifetime, and jet direction at the end of the bubble collapse are investigated. The velocity and pressure fields are also found around the two bubbles in the liquid domain at the end of the bubble collapse.

This numerical modeling considered five distances: $d^* = 2, 2.5, 3, 3.5, \text{and } 4$. In addition, the initial radius is taken $R_0 = 0.165$, and initial pressure $\varepsilon = 100$ and $\gamma = 1.4$ for each bubble. Furthermore, the dimensions of the wall are fixed at 20 R_m long and 10 R_m wide.

6.1 Effect of d^* on bubbles shape, size, centroid movement, and jets

This study analyzes the dynamics of two gas bubbles near a rigid wall. The objective is to understand the effect of the distance between the bubbles on their shape, size, centroid movement, and jets.
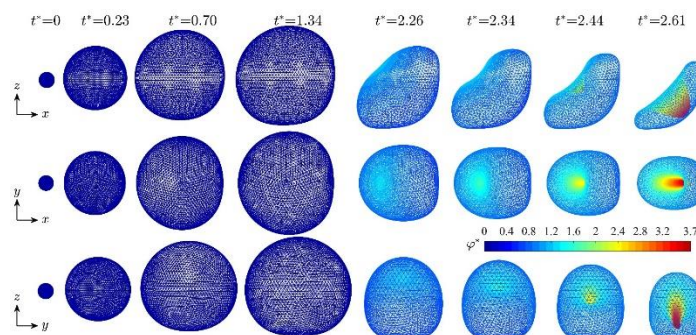
Fig. 4 3D bubble shapes during the expansion and collapse of the left bubble as it oscillates near the right bubble and the horizontal rigid wall with $d^* = 2$, shown from the front view (first row), top view (second row), and side view (third row).

The left bubble shapes during the first oscillation cycle for $d^* = 2$ are shown in Fig. 4 from three viewpoints, which are the front view (xz plane), the top view (xy plane), and the side view (yz plane). It can be seen that the bubble starts to expand from its initial size at $t^* = 0$ and reaches its maximum size at $t^* = 1.34$. The bubble remains spherical at the beginning of the expansion phase because the distances between the bubbles and between the bubble and the rigid wall are still substantial. However, in the final stages of expansion, the bubble surface approaches the right bubble and the rigid wall, by being attracted to them, and thus, loses its spherical shape that is clearly observed at $t^* = 0.70$ and $t^* = 1.34$. The bubble then collapses and a liquid jet is formed at $t^* = 2.34$, which is directed towards the origin. The bubble shape then takes on a kidney-like shape as the jet evolves from the front view. Finally, the jet impacts the far side of the bubble surface at $t^* = 2.61$. The bubble shape during the collapse, as seen from the top view, shows that the bottom part of the bubble extends along the x-axis. Additionally, portion of the bubble near the adjacent bubble extends along the z-axis, which is clearly observed from the side view.

Figures 5 illustrates the shapes and jets of the two gas bubbles near a rigid wall for various

dimensionless distances d^*. Based on Fig. 5 and Table 1, it is observed that the two gas bubbles are positioned symmetrically around the vertical axis at different distances.

In all scenarios, the bubbles exhibit identical shape, size, and movement relative to each other. However, these characteristics are different for different conditions. As d^* increases from 2 to 4, the minimum radius of the bubbles at collapse decreases from 0.511 to 0.419. The lifetime of the bubbles also decreases from 2.606 to 2.470 as d^* increases, while the jet velocity before collapse increases from 4.02 to 4.73. When the bubbles are closely positioned ($d^* = 2$), their centroids move towards each other along the x-axis by 0.128 units and towards the rigid wall along the z-axis by 0.132 units. As d^* increases, movement along the x-axis decreases while movement along the z-axis increases, reaching 0.41 units and 0.201 units respectively at $d^* = 4$.
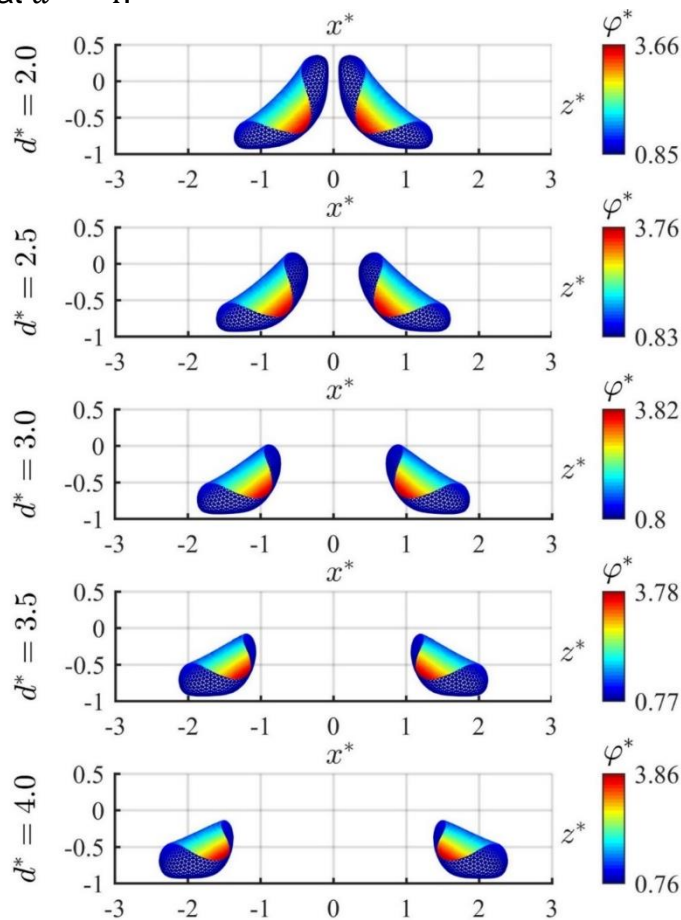
Fig. 5 Bubbles shape for $l^* = -1$ at the jet impact for different

values of d^*.

The jets consistently maintain a nearly spherical shape under all conditions. Their angle changes from 45 degrees for $d^* = 2$ to 70 degrees for $d^* = 2$ relative to the horizontal line, increasingly directed towards the rigid wall as d^* increases. The shape of the bubbles also changes, with the upper part becoming smaller than the lower part near the rigid wall as d^* increases.

The color scale in the figures indicates φ, representing the bubble surface's potential. This potential on the jet surface increases from 3.66 for $d^* = 2$, increasing further in other cases.

Table 1 Jet angle, bubble radius, bubble lifetime, maximum jet velocity, bubble centroid movement along the x and z directions at the final stage of the collapse phase for different distances d^*.

d^*	θ_{jet}	R^*	v^*_{jet}	C^*_x	C^*_z	t^*
2	45°	0.511	4.02	0.128	0.132	2.606
2.5	50°	0.469	4.46	0.103	0.165	2.577
3	57°	0.443	4.55	0.074	0.188	2.546
3.5	62°	0.421	4.71	0.053	0.199	2.506
4	70°	0.419	4.73	0.041	0.201	2.470

According to Table 1 the jet angle in the final stage of collapse increases by 55.55% in the case with $d^* = 2.0$ with respect to th ecase with $d^* = 4.0$. Also, average jet velocity increases by 17.66%, the centroid motion along the z-axis increases by 52.27%, and the potential increases by 5.46%, while the equivalent radius decreases by 18%, the centroid motion along the x-axis decreases by 67.66%, and bubble lifetimes decreases by 5.22%.

6.2 Pressure field and velocity vectors for different values of d*

The pressure field and velocity vectors in the liquid around the two bubbles near the rigid wall are calculated on the symmetry plane $y^* = 0$ for all cases $d^* = 2.0, 2.5, 3.0, 3.5$ and, 4.0. Here, the triangulation mesh is used to discretize the plane surface, and the velocity potential values

and pressure on the plane points are determined using Eqs. (9) to (17).

The colors in Fig. 6 represent the pressure field, while the arrows represent the velocity vectors for the case with $d^* = 2$ in xz-plane around the bubbles above the rigid wall. The color bar shows the non-dimensional pressure values. The peak pressures are located above the center of the jets for each bubble, where the maximum pressure reaches 2.6 for this case (Fig. 6a) but the minimum pressure appears in some places between the bubbles that is equal to 0.5 in this case. The velocity vectors revolve around the bubbles and show the jets flow direction.

The area of the peak pressure gradually gets smaller, and its position changes as it moves upward in other cases including $d^* = 2.5, 3.0, 3.5,$ and 4.0 , but the peak pressure increases with d^*. In the case with $d^* = 2.5$ (see Fig. 6b), the peak pressure region deviates slightly from the center of the jet and reaches a value of 3.35, while the velocity vectors has the same magnitude as in the case with $d^* = 2$.

But in the case with $d^* = 3.0$, the shift of the peak pressure upward is shown in Fig. 6c, and reaches a value of 4.36. In this case, the velocity vectors between the bubbles seem to be the same as in previous case and attain their maximum magnitude in jets.

Fig. 6(d) and Fig. 6(e) depict the pressure field velocity vectors in the cases $d^* = 3.5$ and $d^* = 4.0$, respectively, where changes in the peak pressure area and location in these two cases are very clear. The peak pressure in these last cases continues increasing, becoming 5.57 in the case with $d^* = 3.5$, and finally, it rises to 6.43 in the case with $d^* = 4.0$. According to these findings, the peak pressure rises by 147.3% when comparing the scenario with $d^* = 2.0$ to the scenario with $d^* = 4.0$, indicating a substantial change in pressure.
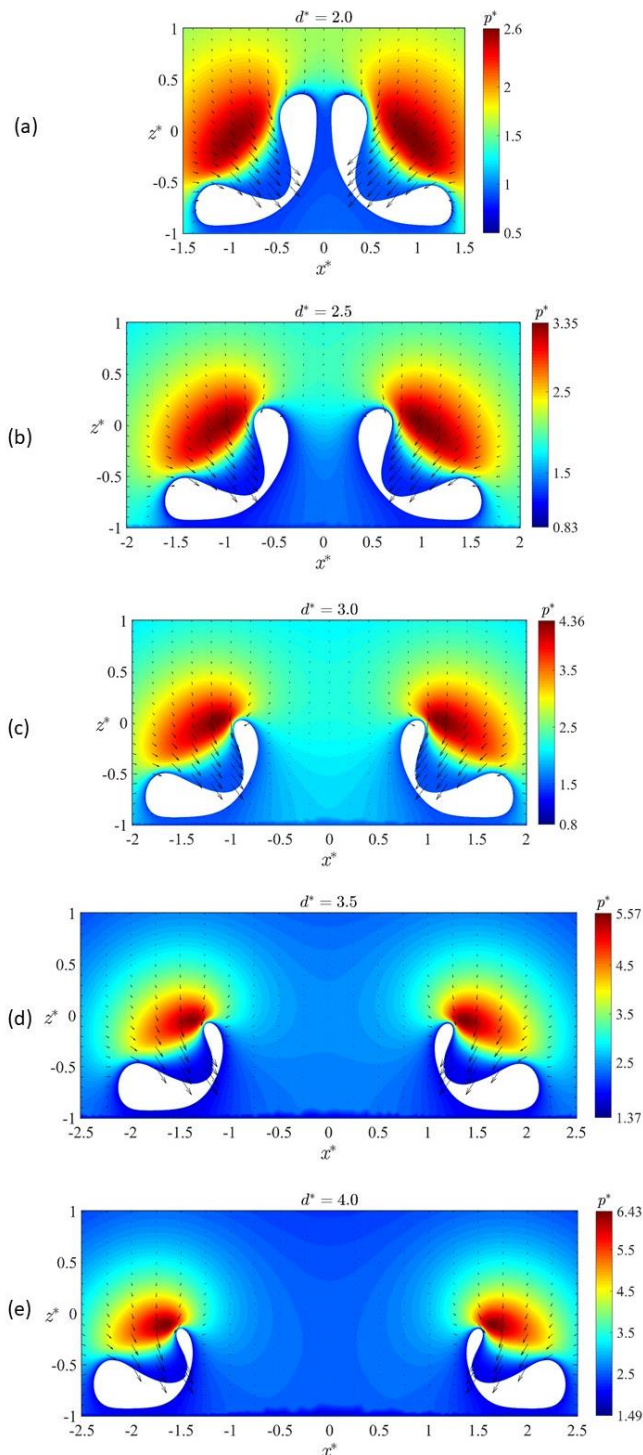
Fig. 6 Pressure field and velocity vectors in the liquid around bubbles for different values of d^*.

7 Conclusions

The Boundary Integral Method (BIM) is used to simulate the dynamics of two 3D bubbles near a rigid wall, employing a local mesh smoothing technique to ensure accurate results. The bubbles remain intact until the final stage of the collapse phase, particularly when positioned in close proximity. Based on our numerical results,

we can conclude the following:

- As the distance (d^*) between the centers of the two bubbles increases, their size decreases while the angle of the jets increases. The jet's shape remains rounded, but the bubbles' shapes become more deformed and less symmetric with increasing d^*. Jets become more inwardly directed and increasingly influenced by the wall as d^* increases.
- Bubble lifetime decreases as d^* increases, correlating with an increase in average jet velocity.
- The centroid movement of the bubbles decreases toward the x-axis but increases toward the z-axis as d^* increases. This indicates that the interaction between the bubbles and the horizontal wall strengthens as the dimensionless distance d^* increases, while the interaction between the bubbles weakens.
- The area of peak pressure for each bubble decreases, while its value increases as the distance d^* increases.

These findings enhance our understanding of bubble dynamics near rigid boundaries and hold potential applications in areas like underwater acoustics, cavitation damage prevention, and microfluidics. Future research could investigate the practical engineering implications of these results.

References

Aziz, I. A., Manmi, K. M., Saeed, R. K. & Dadvand, A. 2019. Modeling three dimensional gas bubble dynamics between two curved rigid plates using boundary integral method. *Engineering Analysis with Boundary Elements,* 109**,** 19-31.

Choi, K., Kim, S., Kim, H. & Kim, C. Influence of the non-isothermal phase change on cavitation bubble dynamics. AIAA SCITECH 2024 Forum, 2024. 2190.

Church, C. C. 1995. The effects of an elastic solid surface layer on the radial pulsations of gas bubbles. *The Journal of the Acoustical Society of America,* 97**,** 1510-1521.

Deane, G. B. & Stokes, M. D. 2002. Scale dependence of bubble creation mechanisms in breaking waves. *Nature,* 418**,** 839-844.

Deen, N. G., Van Sint Annaland, M. & Kuipers, J. 2004. Multi-scale modeling of dispersed gas–liquid two-phase flow. *Chemical Engineering Science,* 59**,** 1853-1861.

Dong, C.-S. & Wang, G.-Z. 2005. Curvatures estimation on triangular mesh. *Journal of Zhejiang University-Science A,* 6**,** 128-136.

Duffy, D. G. 2015. *Green's functions with applications*, Chapman and Hall/CRC.

Ferrara, K., Pollard, R. & Borden, M. 2007. Ultrasound microbubble contrast agents: fundamentals and application to gene and drug delivery. *Annu. Rev. Biomed. Eng.,* 9**,** 415-447.

Han, R., Zhang, A., Li, S. & Zong, Z. 2018. Experimental and numerical study of the effects of a wall on the coalescence and collapse of bubble pairs. *Physics of Fluids,* 30.

Jund, A. A., Dadvand, A., Aziz, I. A. & Manmi, K. M. 2024. An extended Laplacian smoothing for boundary element analysis of 3D bubble dynamics. *Engineering Analysis with Boundary Elements,* 160**,** 76-88.

Katsikadelis, J. T. 2016. *The boundary element method for engineers and scientists: theory and applications*, Academic Press.

Li, Z.-R., Sun, L., Zong, Z. & Dong, J. 2012. A boundary element method for the simulation of non-spherical bubbles and their interactions near a free surface. *Acta Mechanica Sinica,* 28**,** 51-65.

Rypl, D. & Nerad, J. 2016. Volume preserving smoothing of triangular isotropic three-dimensional surface meshes. *Advances in Engineering Software,* 101**,** 3-26.

Saleki-Haselghoubi, N., Dadvand, A., Rasouli, S. & Kadivar, E. 2024. Droplet generation by the oscillation of two spark-generated bubbles near a confined opening. *Engineering Analysis with Boundary Elements,* 159**,** 213-228.

Tanizawa, K. 1995. A nonlinear simulation method of 3-D body motions in waves. *Journal of the Society of Naval Architects of Japan,* 178**,** 96-105.

Tsouris, C. & Tavlarides, L. 1994. Breakage and coalescence models for drops in turbulent dispersions. *AIChE Journal,* 40**,** 395-406.

Wang, C. & Khoo, B. 2004. An indirect boundary element method for three-dimensional explosion bubbles. *Journal of Computational Physics,* 194**,** 451-480.

Wang, C., Khoo, B. & Yeo, K. 2003. Elastic mesh technique for 3D BIM simulation with an application to underwater explosion bubble dynamics. *Computers & Fluids,* 32**,** 1195-1212.

Wang, L., Zhang, Y.-F., Li, H., Sui, Y.-G., Wu, K., Zhang, D.-M. & Yao, W.-H. 2024. Theoretical and numerical studies of the coupled Bjerknes and buoyancy effects on the dynamics of an underwater explosion bubble near a free surface. *Ocean Engineering,* 297**,** 117101.

Wang, Q. & Manmi, K. 2014. Three dimensional microbubble dynamics near a wall subject to high intensity ultrasound. *Physics of Fluids,* 26.

Wang, Q., Manmi, K. & Calvisi, M. L. 2015. Numerical modeling of the 3D dynamics of ultrasound contrast

agent microbubbles using the boundary integral method. *Physics of Fluids,* 27.

Wang, X., Wu, G., Zheng, X., Du, X. & Zhang, Y. 2022. Theoretical investigation and experimental support for the cavitation bubble dynamics near a spherical particle based on Weiss theorem and Kelvin impulse. *Ultrasonics Sonochemistry,* 89**,** 106130.

Wu, G. 1998. Hydrodynamic force on a rigid body during impact with liquid. *Journal of Fluids and Structures,* 12**,** 549-559.

Xi, W. Q. 2004. Numerical simulation of violent bubble motion. *Physics of Fluids,* 16**,** 1610-1619.

Yang, X., Liu, C., Hu, Y., Zhao, M. & Hu, C. 2024. Shock wave induced by the collapse of a bubble cluster with each bubble distributed randomly. *Ocean Engineering,* 300**,** 117362.

Yao, X.-L., Zhang, A.-M. & Liu, Y.-C. 2007. Interaction of two three-dimensional explosion bubbles. *Journal of Marine Science and Application,* 6**,** 12-18.

Ye, X., Yao, X. & Han, R. 2015. Dynamics of cavitation bubbles in acoustic field near the rigid wall. *Ocean Engineering,* 109**,** 507-516.

Zhang, A. & Ni, B. 2014. Three-dimensional boundary integral simulations of motion and deformation of bubbles with viscous effects. *Computers & Fluids,* 92**,** 22-33.

Zhang, A. & Xiong-Liang, Y. 2008. The interaction between multiple bubbles and the free surface. *Chinese Physics B,* 17**,** 927.